buildings

MDPI

Article

Research on Loading Scheme for Large-Scale Model Tests of Super-Long-Span Arch Bridge

Yonghui Fan, Jianting Zhou, Chao Luo, Jun Yang *, Jingzhou Xin and Shaorui Wang

State Key Laboratory of Mountain Bridge and Tunnel Engineering, Chongqing Jiaotong University, Chongqing 400074, China; fyh1995@mails.cqjtu.edu.cn (Y.F.); jtzhou@cqjtu.edu.cn (J.Z.); luochao@mails.cqjtu.edu.cn (C.L.); xinjz@cqjtu.edu.cn (J.X.); ruiruiplace@163.com (S.W.)
* Correspondence: yangjun@mails.cqjtu.edu.cn; Tel.: +86-152-1503-5160

Abstract: A reasonable and efficient loading scheme is needed to guarantee the success of large-scale bridge tests. In this study, an array-type, self-balancing pulley-group loading system was designed based on the world's largest spanning arch bridge using a 1:10 scale model test. Automatic statistics of the required load at each loading point were realized using ANSYS, and a load optimization algorithm for loading points at different construction stages was proposed. Tests were carried out separately for the loading system using a single set of pulley groups and an array-type pulley group. Finite element models of the model bridge and the original bridge were established separately using ANSYS, and the stress results of different components during different construction stages of the main arch ring were compared. The research results show the following: (1) The load magnification factor of the single-pulley-group loading device is approximately 6.6 times, with a mechanical efficiency of 94.26%. (2) In the array-type loading system, the actual load at each loading point can reach the design value. The self-balancing characteristic of this system can eliminate the impact of vertical deformation of the structure on loading accuracy, verifying the reliability of the system. (3) The simulation results of the original bridge and the model bridge coincide well, and the stress of each component during the construction process has the same trend. At key construction stages, the maximum relative errors of the stress results of the rigid steel frame and the concrete inside the pipe of the two bridges are 8.33% and 9.34%, respectively, and the maximum absolute error of the bottom plate concrete is 0.66 MPa, verifying the correctness of the counterweight-optimization method. The loading scheme proposed in this paper can provide a reference for the design of loading systems with the same type of scale model test.

Keywords: rigid-frame arch bridge; scale model test; test design; loading system; weight calculation method

Citation: Fan, Y.; Zhou, J.; Luo, C.; Yang, J.; Xin, J.; Wang, S. Research on Loading Scheme for Large-Scale Model Tests of Super-Long-Span Arch Bridge. *Buildings* **2023**, *13*, 1639. https://doi.org/10.3390/buildings13071639

Academic Editor: Andrea Benedetti

Received: 15 May 2023
Revised: 22 June 2023
Accepted: 27 June 2023
Published: 27 June 2023

1. Introduction

According to available data, all concrete arch bridges featuring a span exceeding 300 m worldwide utilize rigid-frame arch bridge structures [1]. The Tian'e Longtan Grand Bridge, which is presently under construction, boasts a main span reaching an impressive 600 m. With an increase in span for rigid-frame arch bridges, structural stress becomes increasingly complex [2], necessitating advanced requirements for bridge design principles and construction control methodologies. Scaled model experimentation serves as an efficacious approach to ascertain the genuine structural status of arch bridges under load-bearing circumstances [3], providing benefits such as elevated safety, robust control over test conditions, and abbreviated test durations.

Researchers have conducted studies on many large bridges around the world [4–7] focusing on the design of scaled bridge tests. The efficiency and accuracy of the loading system, as an essential component of scaled bridge tests, are some of the critical factors affecting the success of these experiments. Currently, research on loading systems in scaled

bridge tests conducted by scholars both domestically and internationally can be roughly divided into three categories:

1. The first category mainly uses hydraulic jacks for loading. The base of the hydraulic jack is fixed to the ground or another rigid structure, and the load is applied to the structure through the jack head. This loading method is suitable for cases with fewer loading points and shorter loading cycles [8]. For example, Liu et al. [9] conducted a 1:16 scale test of the Wasiwo Bridge which has a clear span of 95 m, studying the failure modes of catenary arches under loading at the crown and L/4 span. Wang et al. [10] proposed a double-layer corrugated steel–concrete composite arch structure and studied the bearing capacity of this type of arch using a single-point loading test at the mid-span.
2. The second category is the multi-point suspended-weight method, which applies the self-weight of counterweights as the load on the structure. For example, Liu et al. [11] used 32 tons of iron bars to load a model test to study the mechanical behavior of a steel truss arch bridge. This method results in large counterweight volumes, occupying a significant amount of experimental space and affecting the normal use of other test equipment. Li et al. [12] investigated the dynamic response of a long-span, irregular steel tube-reinforced concrete arch bridge. They conducted 1:16 scale model tests of the Yitong River Bridge with a main span of 158 m. The test was designed to simulate vehicle loads using iron bricks to simulate the self-weight of the bridge. However, due to space limitations, it was not possible to achieve an equivalent weight loading of the self-weight.
3. To solve the problems of large counterweight space and high counterweight cost, some scholars have designed a third category of loading systems, the lever method. This method uses the principle of moment balance to multiply the self-weight load of the counterweight acting on the structure to be loaded. For example, Zhang et al. [13] conducted a 1:7.5 scale model test of the main arch ring of the 445-m main span of Beipan River Bridge, which is a rigid-frame arch bridge. Based on the lever principle, 48 sets of loading devices were used to achieve the equivalent counterweight of the arch rib. Tang et al. [14] conducted a 1:10 scale model test of the main arch ring of the 420-m main span of Wanxian Yangtze River Bridge, studying the feasibility of the main arch ring's formation sequence and the rationality of the internal force and deformation during the construction stage. The test achieved rib weighting at 27 loading points using the lever principle, but this method increased the workload of the weighting process as the vertical deflection of a loading point would change the load of adjacent loading points in real time, thus making it challenging to ensure the accuracy of the rib weighting at each loading point, which significantly affected the accuracy of the model test results in terms of inferring the bridge's response from the model test [15].

In summary, traditional model test loading systems have limitations, such as limited loading point numbers, large counterweight volumes, and low loading accuracy [16–19]. To address these issues, a 1:10 scale model loading system for the main arch ring of the 600-m main span of Tian'e Longtan Grand Bridge was designed. An innovative array-type, self-balancing pulley-group loading system and counterweight optimization algorithm were proposed. This loading system offers advantages, including small counterweight volume, long-term stability, elimination of repeated adjustments during multi-point loading, and high loading accuracy. Our aim is to provide a reference for the design of reduced-scale model tests for similar bridges in the field of engineering structures, overcoming the aforementioned limitations in existing loading systems.

2. Test Overview

2.1. Overview of the Original Bridge Project

The Tian'e Longtan Grand Bridge is an upper-bearing, steel tube-reinforced concrete rigid-frame arch bridge, with a main span of 600 m, a rise of 125 m, and a rise-to-span

ratio of 1/4.8 [20], as shown in Figure 1. The main arch curve is in the form of a catenary, with an arch axis coefficient of m = 1.9. The arch ring adopts a concrete box section with constant width and variable height, with a box width of 6.5 m, a box height of 12 m at the arch foot, and a box height of 8 m at the arch crown. The transverse center distance of the arch rib is 16.5 m, and the thickness of the arch box web gradually changes from 0.45 m at the arch crown to 0.95 m at the arch foot. The top slab thickness is 0.65 m, and the bottom slab thickness gradually changes from 0.65 m at the arch crown to 1.3 m at the arch foot. The rigid steel skeleton primarily uses Q420 steel, while the internal concrete employs C80 self-compacting micro-expansion concrete, and the external concrete utilizes C60 concrete. Notably, the external concrete is cast using a segmented ring method, dividing the external concrete horizontally into three rings, including the bottom slab, the web, and the top slab, and adopting a symmetrical casting approach with eight working faces longitudinally.

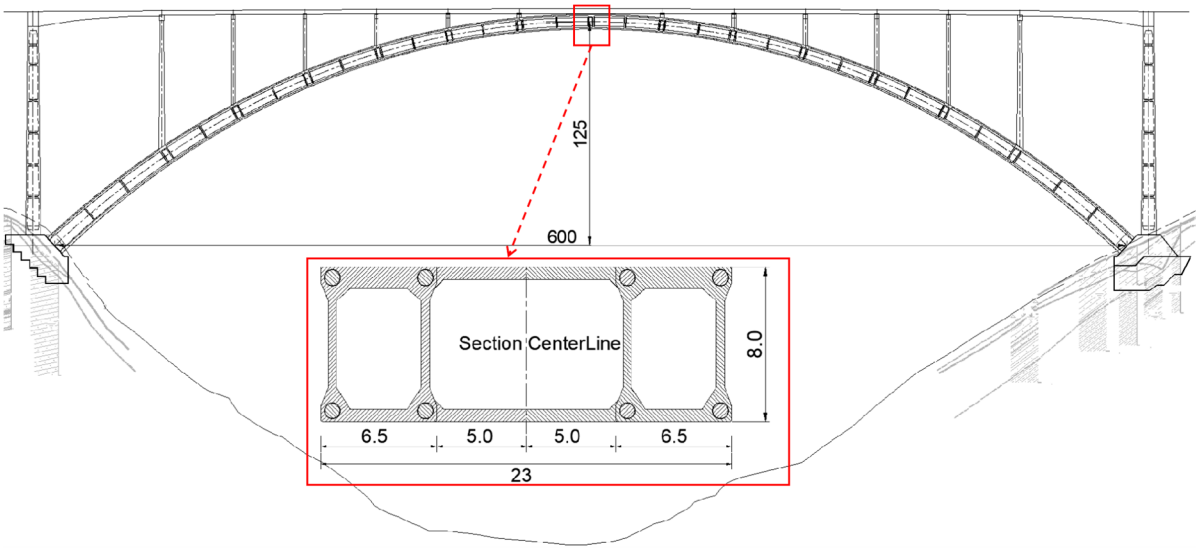

Figure 1. Elevation view of Tian'e Longtan Grand Bridge (unit: m).

2.2. 1:10 Scale Model Test of the Main Arch Ring

A 1:10 scale model experiment was conducted on the main arch ring of the original bridge, with stress equivalence as the design principle [21,22]. To minimize the influence of the scale effect on the structural response [23], the overall geometric parameters of the model bridge, such as span and rise, were strictly converted according to the scale ratio. Local designs adhered to the principle of achieving rigidity similarity and construction requirements in order to replicate the actual project conditions to the greatest extent and to strive for consistency of stress conditions between the model bridge and the original bridge. Additionally, by conducting nearly one hundred sets of experiments on the concrete mix ratio, we ensured that the concrete material properties of the model bridge closely resembled those of the original bridge [24], thereby reducing the potential impact of the scale effect on the material side.

It is important to note that the scale effect primarily affects discontinuous regions where beam theories [25], such as the Euler–Bernoulli beam theory, are not applicable. However, in the context of the present experiment, the rigidity of the skeleton structure remains continuous throughout the investigation process. When integrated with the results from Section 4.3, it becomes evident that the scale effect has not significantly impacted the precision of our experimental outcomes.

2.2.1. Scaled Model Test Scheme

The model test was carried out in the State Key Laboratory of Mountain Bridges and Tunnel Engineering at Chongqing Jiaotong University, with a main span of 60 m, as shown

in Figure 2. This span exceeds the largest scaled test ever conducted for similar bridge types [14,26], making it the largest scaled model test for an arch bridge in the world to date.

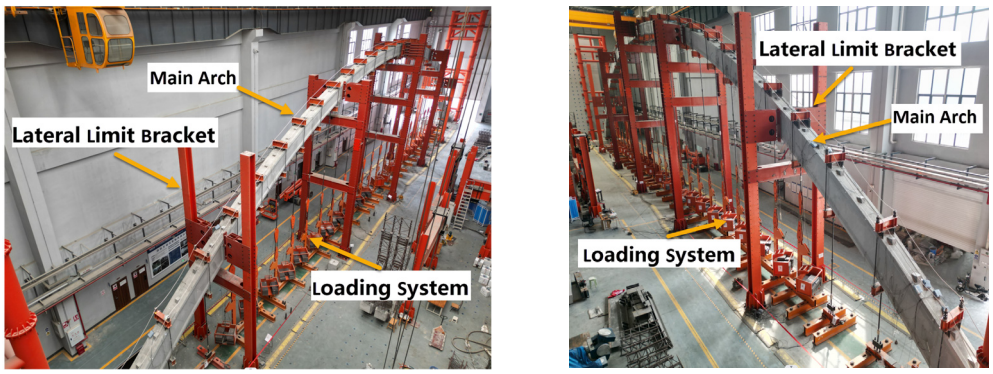

(**a**) (**b**)

Figure 2. Picture of model test. (**a**) Figure of the arch bridge model test under viewpoint 1; (**b**) Figure of the arch bridge model test under viewpoint 2.

This structure's arch axis adopts a catenary, with an arch axis coefficient (m) of 1.9, a calculated rise of 12.5 m, and a span-to-rise ratio of 1/4.8. The arch rib adopts a concrete box-type section with uniform width and variable height, as shown in Figure 3. The box is 0.65 m wide, the box height at the foot of the arch is 1.23 m, and the box height at the apex of the arch is 0.83 m. The thickness of the box web plate gradually varies from 55 mm at the apex to 95 mm at the foot of the arch. The top plate is 65 mm thick, while the bottom plate thickness gradually varies from 65 mm at the apex to 130 mm at the foot of the arch. To enhance the local stability of the main arch ring, transverse partitions with a thickness of 50 mm are arranged every 2 m along the length of the bridge.

The model test's main arch ring mainly includes three parts: a rigid steel framework, C80 internal concrete in the pipe, and C60 external concrete. The rigid steel framework was assembled using the large-section lifting method, with a total weight of approximately 5.0 tons. The internal concrete was pumped from both sides of the arch base section symmetrically toward the arch crown using the pumping and jacking method, with a total volume of approximately 1.5 m^3.

The casting of the external concrete is consistent with the original bridge, dividing the external concrete into three rings in the transverse direction: the bottom plate, the web, and the top plate. In the longitudinal direction, each ring is divided into eight working faces, with each working face being divided into six segments for casting. The model test's segmented positions and the casting length of each segment are consistent with the original bridge, which has been scaled proportionally, and the age difference between the concrete segments is basically the same as the original bridge.

The main test content of this experiment included the strain, displacement, environmental temperature fields, and structural temperature field throughout the construction process [27]. The strain testing primarily involved the establishment of test cross-sections at 16 longitudinal points of the bridge (a total of 17 test sections are shown in Figure 4a), with fiber-optic strain sensors being arranged at each cross-section on the main steel tube, bottom plate, web, and top plate, as shown in Figure 4a. The displacement testing was mainly conducted at 8 longitudinal points of the bridge (a total of 7 test sections are shown in Figure 4b), with four measurement points set near the upper and lower chord steel tubes at each cross-section. The related testing was completed using wire-drawing displacement sensors, as shown in Figure 4b. The environmental temperature field and structural temperature field were monitored using PT100 sensors. Given that the temperature distribution of the lab environment and the structure was relatively uniform, an environmental temperature sensor and a structural temperature sensor were placed along the bridge longitudinally at intervals of 10 m.

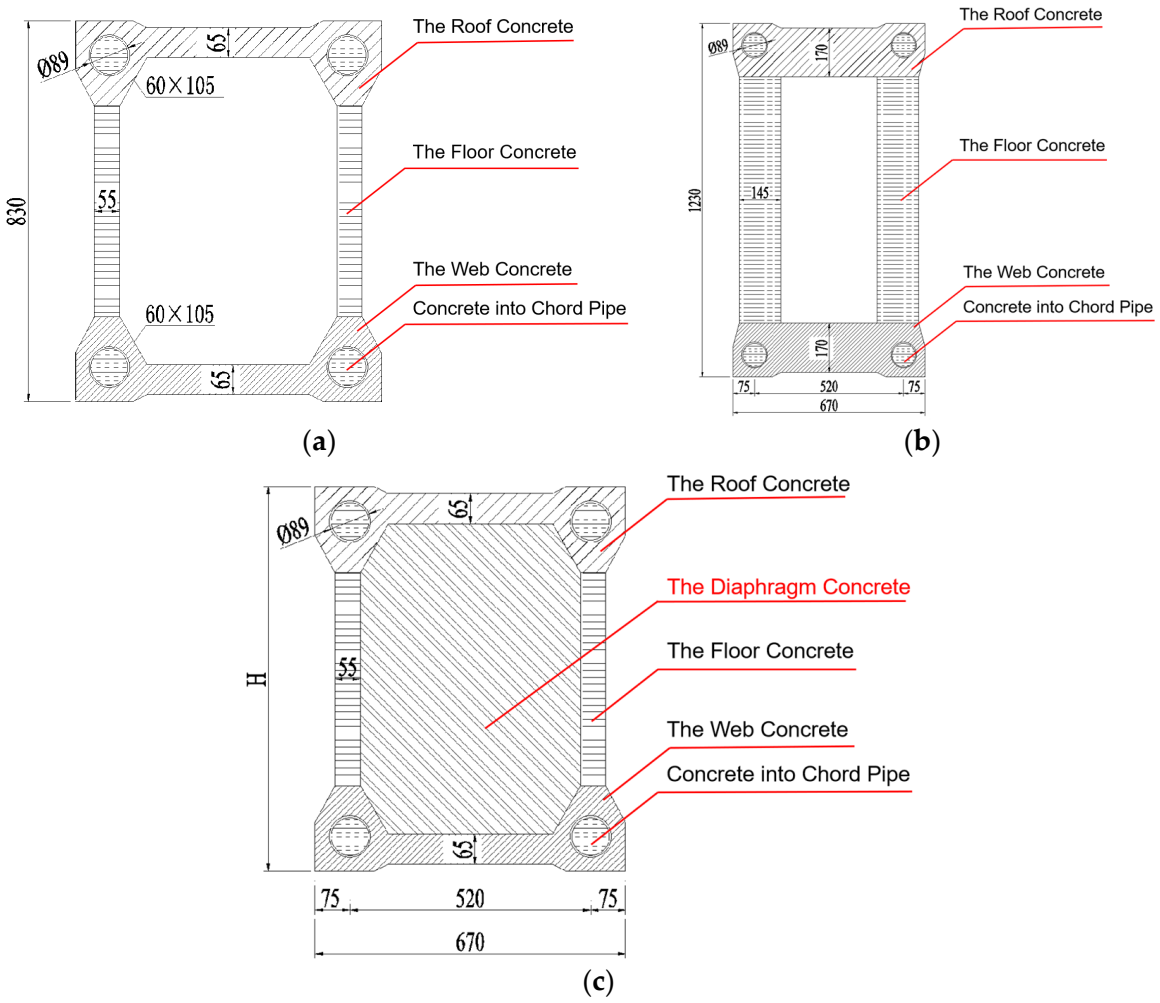

Figure 3. Cross-section of the main arch ring of the model bridge (unit: mm). (**a**) Dimensional drawing of mid-span section; (**b**) Dimensional drawing of arch foot section; (**c**) Dimensional drawing of the cross-section of the mid-span diaphragm.

2.2.2. Model Test Construction Stages

By referring to the original bridge's construction process, the construction of the main arch ring is divided into 20 stages, with the specific content of each stage shown in Table 1.

Table 1. Division of the construction stages of the main arch ring.

Serial Number	Construction Content
1	Closure of rigid steel frame
2	Pouring concrete into the pipe
3~8	Pouring concrete for base slab
9~14	Pouring web concrete
15~20	Pouring roof concrete

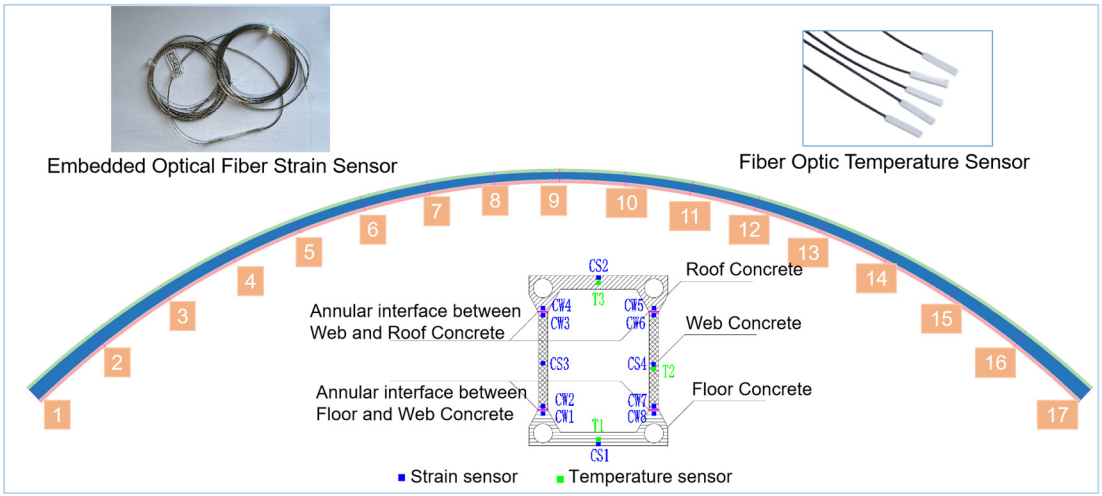

(**a**)

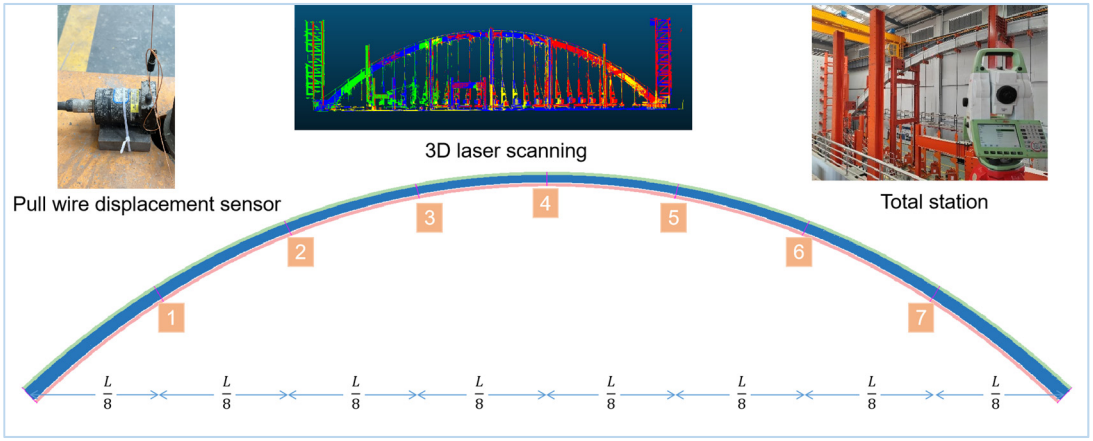

(**b**)

Figure 4. Schematic diagrams of test cross-sections and test methods. (**a**) Cross-section of strain test and sensor display diagram; (**b**) Displacement testing cross-section and display diagram of testing equipment.

3. Loading System Design

The model test was designed based on the principle of stress equivalence. Under a scale factor of 1:10, a nine-time self-weight load should be applied to the model arch. The self-weight load is approximately uniformly distributed along the longitudinal direction of the main arch ring. Theoretically, the nine-time self-weight load should also be applied as a uniformly distributed load. Considering the available space in the laboratory, operational feasibility, and finite element calculation results, a loading point was arranged every 2 m along the bridge's longitudinal direction, using 29 concentrated forces to replace the uniformly distributed load. To prevent local buckling or distortion buckling of the structure near the loading points during the construction stage, a transverse partition was set up at each loading point section.

3.1. Loading Scheme

3.1.1. Working Principle of Single-Point Loading Device

Reasonable and accurate counterweights directly affect the accuracy of the test data, and an efficient and feasible counterweight method is an important part of the test design. To solve the drawbacks of traditional loading methods, a pulley-group loading scheme was designed [28–30], and its working principle is shown in Figure 5. In the figure, pulleys X1, X2, and X3 form a fixed pulley group, which is fixed on the ground, and pulleys S1, S2, and

S3 form a movable pulley group, which is connected to the upper structure using elastic supports to simulate the vertical displacement of the main arch ring. The pulley groups are connected by a wire, starting from the axis of pulley S3, winding counterclockwise around pulleys X1, S3, X2, S2, X3, and S1 in sequence, and a counterweight block is suspended at the end of the wire.

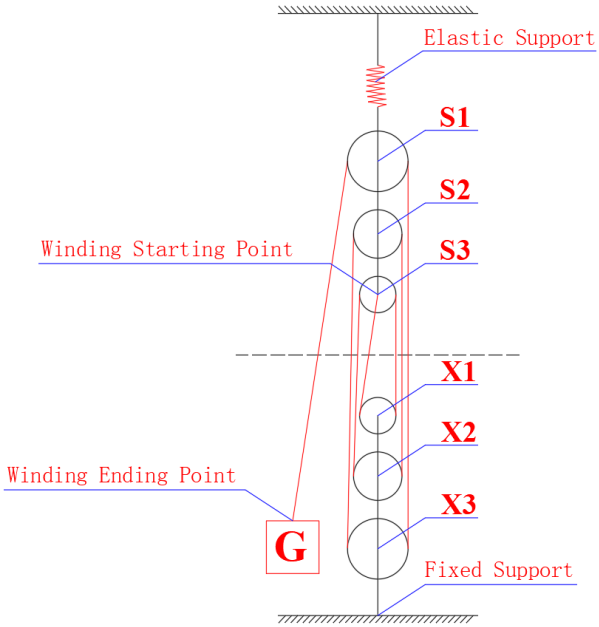

Figure 5. Diagram of the working principle of a loading system with a single set of pulleys.

In the aforementioned loading scheme, the ratio of the actual load (F) borne by the loading point to the self-weight load (G) of the counterweight block is denoted as the load magnification factor, represented by F_S. The schematic calculation diagram is shown in Figure 6. In Figure 6, taking pulley S2 as the research object, the load magnification factor $F_2 = F_6$ can be determined according to the principle of moment balance. By analogy, $F_i = G(i = 1, 2, \cdots, 7)$ can be obtained; thus, the theoretical value of the load magnification factor for the single-point loading device under this design scheme can be derived as follows:

$$F_S = \frac{F}{G} = \frac{\sum_{i=1}^{7} F_i}{G} = 7 \tag{1}$$

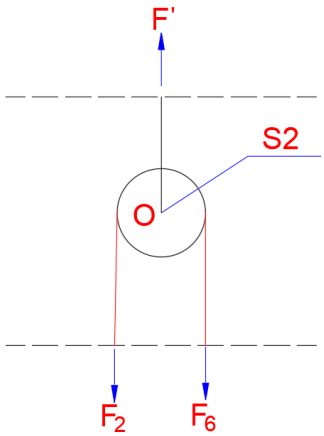

Figure 6. Simple diagram of single pulley force.

For the moving pulley system, the load magnification factor, F_S, alters along with the changes in the number of pulleys, and the relationship between the two is expressed as follows:

$$F_S = 2X_m + 1, (X_m \in N_+) \quad (2)$$

where X_m represents the number of moving pulleys.

It is worth noting that as the number and the diameter of the pulleys increase, the total frictional force between the pulleys and the rope will also escalate, causing a reduction in the mechanical efficiency of the single pulley system's loading apparatus. Simultaneously, a rise in frictional force extends the time required for the tension of the outer wire rope to reach the inner wire rope. Therefore, when designing an experiment, comprehensive consideration should be given to various factors, such as the load magnification factor, mechanical efficiency, and the time required for the system to stabilize.

3.1.2. Design Scheme of Loading Device with a Single Set of Pulley Group

Following the design principle discussed in the previous section, the design of the single-pulley-group loading device was completed, as shown in Figure 7. In this apparatus, the movable pulley group is connected to the main arch ring through the main arch ring's fixture and connecting rod. The stationary pulley group is connected to the ground using the lower jig and the lower jig base. Both pulley groups consist of three steel pulleys, with diameters of 310 mm, 230 mm, and 130 mm, respectively. The steel wire rope has a diameter of 8.7 mm. A counterweight box is used to house the counterweights, allowing sequential loading based on experimental requirements. The tension sensor can display and record the load values at the loading points on the main arch ring in real time.

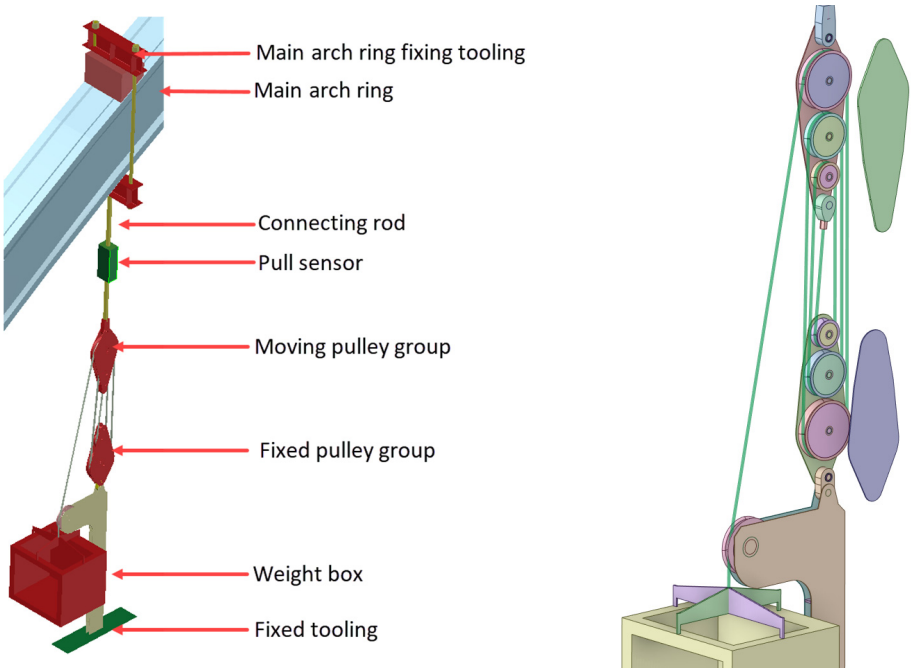

Figure 7. Schematic diagrams of a single-pulley-group loading system. (**a**) Overall diagram of a loading system with a single set of pulley group; (**b**) Partial view of a loading system with a single set of pulley group.

3.1.3. Loading System's Overall Layout Scheme

In accordance with the experimental requirements, the loading devices described in the previous section were sequentially arranged along the longitudinal direction of the bridge, forming an array-based pulley-group loading system, as shown in Figure 8. In this system, even if the counterweight near the loading point affects the vertical displacement of

the current loading point, due to the equal tension on both sides of the same pulley's steel wire rope, the load amplification factor of the current loading point will gradually approach seven times over time, exhibiting a self-balancing characteristic. This system overcomes the shortcomings of the hydraulic jack-loading method, in which the load values are difficult to maintain stable over a long period; the lever-loading method, where load values are easily affected by adjacent loading points; and the direct-counterweight method, where the counterweight blocks are excessively large in volume.

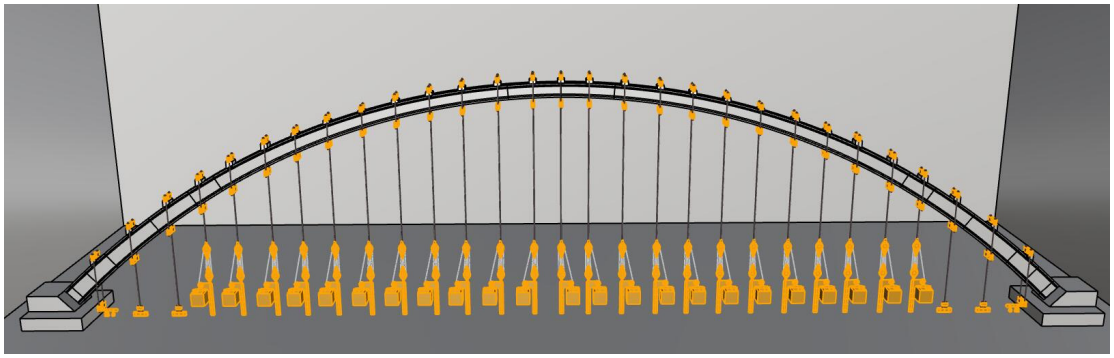

Figure 8. Overall layout plan of the model test's loading system.

3.2. Array-Based Loading System's Load Calculation Method

3.2.1. Load Point Counterweight Calculation Intervals

The main arch ring has a cross-section with constant width and varying height, and the thickness of the external concrete at different longitudinal positions is not the same. It would be unreasonable to simply distribute the weight of the main arch ring evenly among the various loading points. Instead, the counterweight should be calculated and allocated based on the actual size and weight of the structure near each loading point. The specific calculation method is as follows:

Let the longitudinal coordinates of the centroid of the arch springing plane on the left and right arch feet be 0 and 60, respectively. Denote the longitudinal coordinates of the 29 loading points from left to right as $X = \{X_1, X_2, \cdots, X_{29}\}$, and the longitudinal coordinates of the midlines between adjacent loading points as $x = \{x_1, x_2, \cdots, x_{28}\}$. We have

$$x_i = (X_i + X_{i+1}) \times 0.5, \quad (i = 1, 2, \cdots, 28) \tag{3}$$

The counterweight value F for the ith loading point is

$$F_i = \begin{cases} 9 \times G_j(0, x_1) & , i = 1 \\ 9 \times G_j(x_i, x_{i+1}) & , i = 2, 3, \cdots, 28 \quad (j = 1, 2, \cdots, 22) \\ 9 \times G_j(x_{28}, 60) & , i = 29 \end{cases} \tag{4}$$

In the formula, $G_j(x_i, x_{i+1})$, $(x_i, x_{i+1} \in [0, 60])$ represents the total self-weight of all constructed components within the range of the centroid longitudinal coordinates (x_i, x_{i+1}) during the jth construction stage.

3.2.2. Counterweight Values of Each Loading Point at Different Construction Stages

The model bridge is divided into 20 construction stages. Manually calculating the counterweight loads of the 29 loading points at different construction stages would be a massive workload. In this study, the ANSYS APDL [31] programming language was utilized to develop a set of counterweight load calculation programs, which can automate the aforementioned task. The basic process is shown in Figure 9.

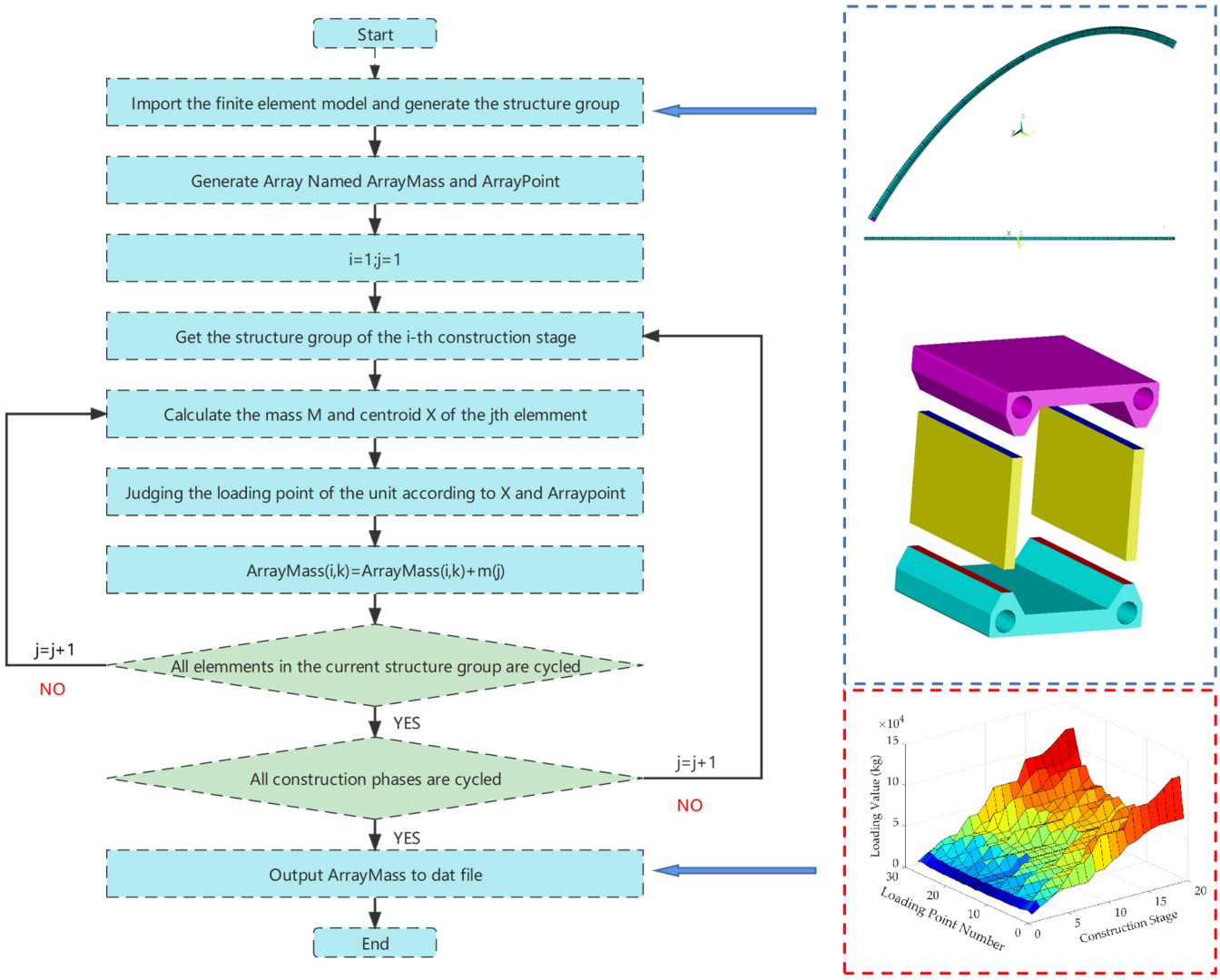

Figure 9. Flow chart of counterweight statistics at each loading point.

In Figure 9, ArrayMass is a 20 × 29 two-dimensional array, with the first dimension used to store construction stage information and the second dimension used to store loading point numbers; ArrayPoint is a one-dimensional array with 28 elements, and $x = \{x_1, x_2, \cdots, x_{28}\}$ is used to store information; i represents the construction stage, taking $i \in \{1 \leq i \leq 20 | i \in N^+\}$; and j represents the element number in the finite element model, taking $j \in \{1 \leq j \leq 6660 | j \in N^+\}$.

3.2.3. Optimization of Load Application Points' Weighting Values

In comparison to the original bridge, the model bridge design exhibits an increase of 12.30~30.27% in the cross-sectional areas of steel tubes, an increase of 7.42~23.77% in the chord members in the cross-sectional areas, a thickening in specific regions of the external concrete web, and additional thickening of the concrete near the steel tubes. Applying a nine-fold weighting value as per the model bridge would be unreasonable; thus, optimization of the weighting values for each load application point at various construction stages is required.

Given that the design of the model bridge, in comparison to the original bridge, only features scaling up without scaling down, the load value at each application point is determined based on the model bridge. These load values exceed the theoretical weighting values for the original bridge after scaling down, which prompts the introduction of the concept of a weighting reduction factor. This factor is defined as the ratio of the required

weighting values for the actual model test design and the original bridge at a 1:10 scale without any modifications to component dimensions. During calculations, the following principles should be followed for the weighting reduction factor:

(1) Weighting calculations for components participating in the overall structural force, such as the main steel tubes and inner concrete of the rigid steel framework, should be nine times their actual dimensions.
(2) Weighting calculations for components participating in localized structural forces, such as the steel framework web members and top and bottom transverse links, should be nine times their actual dimensions after scaling down the original bridge components.
(3) As the rigid framework forms an arch in stages, the reduction factors at different construction stages for each load application point vary and should be calculated separately.
(4) In the model test, the weighting at each load application point is progressively applied as the construction stage advances. When calculating the weighting reduction factor, component parameters involved in the calculation should only be taken from newly poured components at the current construction stage, as the previous stage's weighting has been completed and should no longer be included in the early-stage weighting results.

Thus, in the *i*th construction stage, the weighting reduction factor $P_s(i, j)$ for the *j*th load application point can be calculated using the following formula:

$$P_s(i,j) = \frac{\sum \rho_1 A_1 + \sum \rho_2 A_2}{\sum \rho_0 A_0} \tag{5}$$

In this formula, $\sum \rho_0 A_0$ represents the sum of the product of the component area and the corresponding material density near the *j*th load application point of the model bridge in the *i*th construction stage; $\sum \rho_1 A_1$ represents the sum of the product of the overall force-bearing component area and the corresponding material density near the *j*th load application point of the model bridge in the *i*th construction stage; and $\sum \rho_2 A_2$ represents the sum of the product of the cross-sectional area and the corresponding material density of the original bridge's localized force-bearing components, which have been scaled down to 1:10, near the *j*th load application point in the *i*th construction stage.

4. Reliability Verification of the Loading System

4.1. Test of Loading System with a Single Set of Pulley Group

To verify the reliability and mechanical efficiency of the loading device, the loading system with a single set of pulley group was selected for the staged loading test, as shown in Figure 10.

In this system, the horizontal beam of the portal frame is used as a substitute for the main arch ring. Gradual loading is achieved by placing 40 cm × 40 cm × 2 cm steel plates in the counterweight box. During the test, the loading was divided into four stages, with each stage having loads of 0.2 t, 0.4 t, 0.6 t, and 0.8 t, respectively. After the loading was completed, the total mass of the counterweight box was 2.0 t. By reading real-time data from the load cell, the actual amplification factor of the pulley-group loading system can be obtained. The results are shown in Figure 11.

As shown in Figure 11, after each loading is completed, the load magnification factor of the single-pulley-group loading device requires approximately 10 min to reach a stable state. This is because the steel wire rope needs to overcome the resistance at the pulley to transmit the tension of the outermost steel wire rope layer by layer to the innermost steel wire rope. This process is referred to as the hysteresis effect. It is this effect that causes the load magnification factor to suddenly drop during each loading, as indicated by points A, B, C, and D in the figure. Moreover, after the completion of each loading level, the load magnification factor remains relatively stable around 6.6 times, indicating that the

mechanical efficiency of the single-pulley-group loading system is approximately 94.29%, meeting the test requirements. Additionally, the influence of friction loss on the loading value can be eliminated based on the specific readings of the tension sensor.

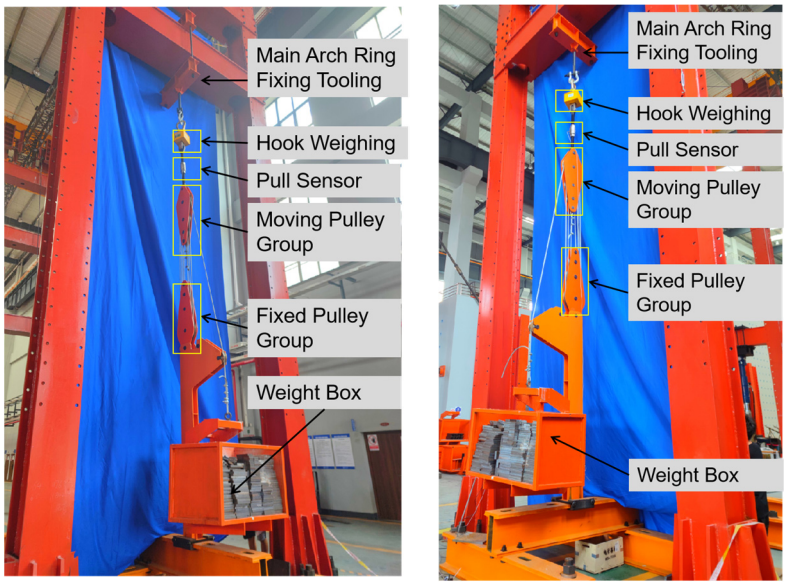

(**a**) (**b**)

Figure 10. Test of loading system with a single set of pulley group. (**a**) Loading system with a single pulley set under viewpoint 1; (**b**) Loading system with a single pulley set under viewpoint 2.

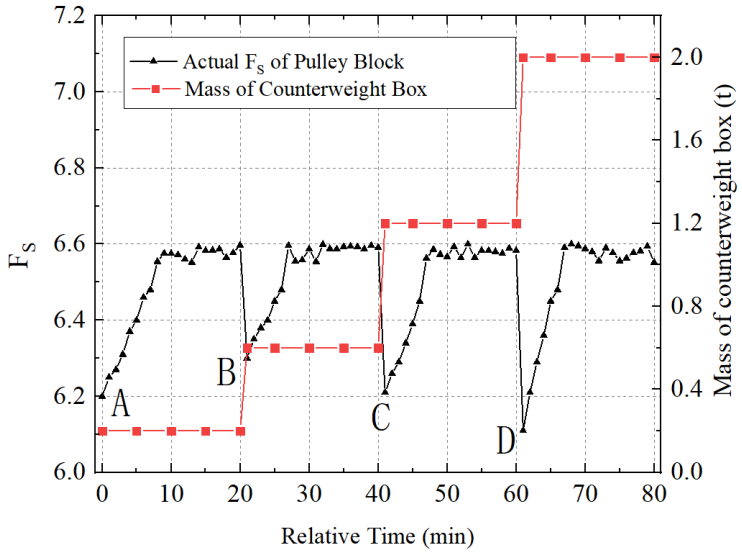

Figure 11. Time load curve of the loading test.

4.2. Array-Type Pulley-Group Loading System Test

To verify the reliability and stability of the array-type loading system in practical applications, selected loading points during the external concreting stage of the model test were chosen, and their design load values are presented in Table 2. The Donghua DHDAS data acquisition system was employed to collect real-time counterweight data of the relevant loading points, and the results are shown in Figure 12.

Table 2. Design loading value of selected loading points.

Number of Loading Points	Value of Theoretical Weight (kg)	Load Order
6#	1069	1
11#	982	2
15#	2320	3

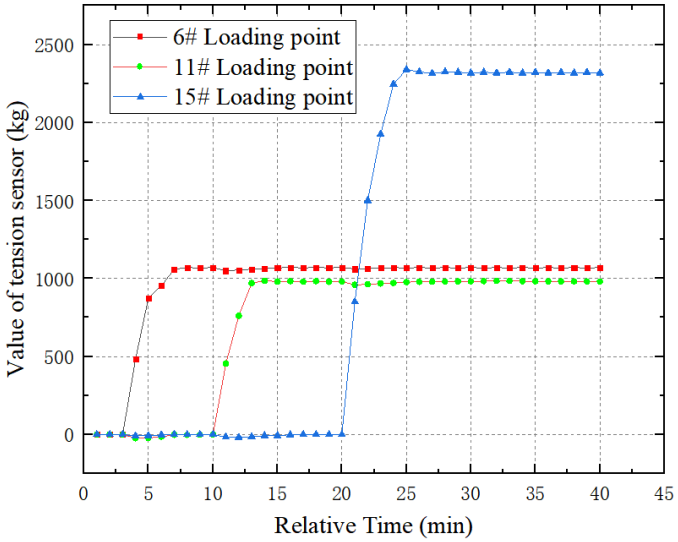

Figure 12. Time load curve of each loading point.

As shown in Figure 12, approximately 5 min after each loading point has completed loading, the values of the tension sensors can reach the designed load and remain relatively stable. Moreover, the load value of the *i*th loading point is affected by the *j*th loading point. This is because the counterweight of the latter causes a vertical deflection at the loading position of the former. This deflection is transmitted to the movable pulley group, causing the movable pulley group and the fixed pulley group to move closer together, which results in a certain degree of slack in the steel wire rope and a decrease in the total load value. However, after about 5 min, the load at each point returns to the original load due to the equal tension of the steel wire rope on both sides of the same pulley, demonstrating that the self-stabilizing characteristic of the system causes the mutual influence between the loading points to diminish over time. This confirms that the array-type pulley-group loading system exhibits good stability and high reliability.

4.3. Comparison of Finite Element Simulation Results

To verify the correctness of the load optimization algorithm for the array-type self-balancing pulley-group loading system, finite element models of the original bridge and the model bridge were established using the ANSYS APDL 18.0 software [30], as shown in Figures 13 and 14. In both cases, the rigid steel skeleton and internal concrete were simulated using Beam188 elements, while the external concrete was simulated using Shell181 elements. The displacement and rotation of both arch feet were constrained, and the construction process was simulated using birth and death elements. During calculations, only the self-weight load was considered for the original bridge, whereas the model test bridge considered not only the self-weight load but also the vertical load applied by each pulley-group loading device on the structure.

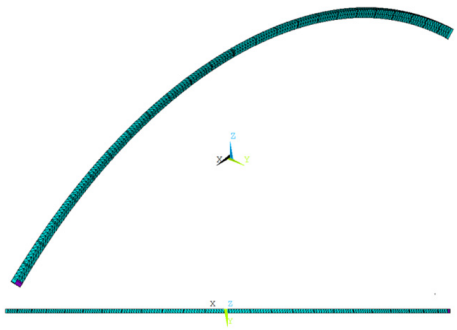

Figure 13. Finite element model of the main arch ring in the model test.

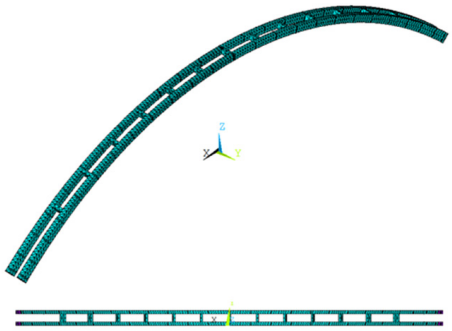

Figure 14. Finite element model of the main arch ring of the original bridge.

The stress values of the main steel tubes, internal concrete, and external concrete in the rigid steel skeletons of the original bridge and the model test bridge at key sections during the construction process were extracted and compared. Some of the results are shown in Figure 15.

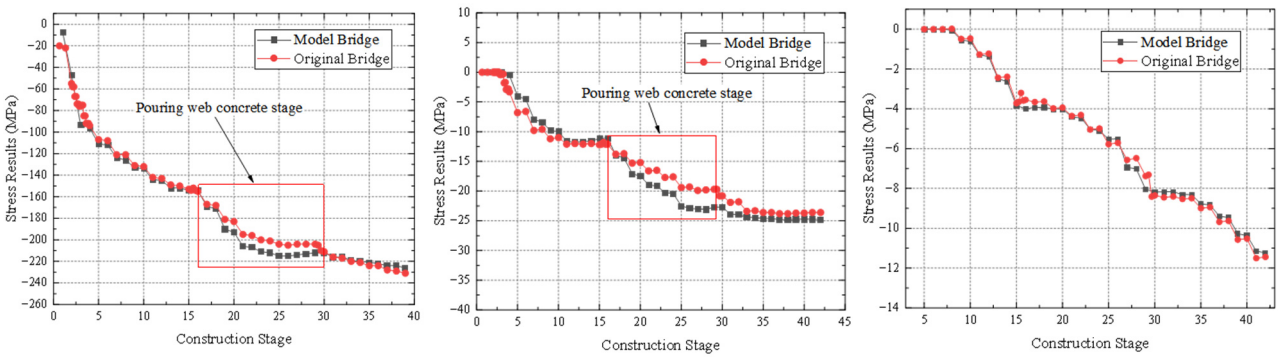

Figure 15. Comparison of the theoretical stress results of different components of the original bridge and the model test bridge. (**a**) stress results of the upper chords of 3/16-span sections; (**b**) stress results of the upper chord of 1/4 span sections; (**c**) stress results of the roof concrete of 1/4 Spans sections.

In Figure 15, the stress results of different components of the model bridge and the original bridge exhibit similar trends at various construction stages. During the web concrete pouring stage, the stress results of the model bridge are slightly larger than those of the original bridge. This is because the web concrete thickness of the original bridge, which is 45 cm, was scaled down to only 45 mm, making it difficult to arrange the reinforcement. For construction safety, the web concrete thickness in this area was increased to 55 mm, resulting in an increased self-weight load of the scaled-down web concrete and, ultimately, slightly higher stress results for the model bridge during this construction process.

In Figure 15a, the stress of the rigid steel skeleton has a larger difference during the 2–3# construction stages, while the maximum difference in the other construction stages is 8.33%. This difference arises from the fact that, for safety reasons, the model test did not apply loads after the rigid steel skeleton was connected; instead, the counterweights were applied after the internal concrete was poured. Considering that the focus of the model test is on the structural state during the external concrete process, and subsequent construction stages show good agreement between the two stress results, the stress difference during the internal concrete pouring stage can be ignored. In Figure 15b, the maximum stress deviation between the model bridge and the original bridge for the main arch ring, excluding the web concrete pouring stage, is 9.34%. As shown in Figure 15c, the stress trends of the bottom slab concrete construction stages for the model bridge's and original bridge's main arch ring are essentially the same, with a maximum stress difference of 0.66 MPa. These results indicate that the model bridge's main arch ring can adequately reflect the stress state of the original bridge during construction, verifying the correctness of the load optimization algorithm for the array-type, self-balancing pulley-group loading system.

5. Conclusions

A 1:10 scale model test was conducted based on the Tian'e Longtan Grand Bridge with a main span of 600 m. Considering the shortcomings of traditional loading methods in the test design process, an array-type, self-balancing pulley-group loading system was designed. This system was introduced, tested, optimized, and compared with the finite element simulation calculations. The main conclusions are as follows:

(1) A single set of loading devices based on the pulley-group design can theoretically amplify the dead weight of the counterweight box by seven times, which can be applied to the loading point. Multiple sets of loading devices arranged longitudinally along the bridge can form an array-type, self-balancing pulley-group loading system, which does not require repeated load adjustments, offers high precision in counterweight values, and occupies less space.

(2) A calculation method for the counterweight value at any loading point at different construction stages was proposed, and automation of load statistics was achieved using the ANSYS APDL language. Considering the differences in the detailed dimensions between the model bridge and the original bridge, the calculation principle of the counterweight reduction factor was proposed, thereby optimizing the counterweight calculation method when designing the arch bridge model test according to stress equivalence.

(3) A counterweight test of loading devices with a single set of a pulley group was conducted, revealing that due to the friction between the pulley and the steel wire rope, the actual load magnification factor of the loading devices is approximately 6.6 times, with a mechanical efficiency of about 94.29%.

(4) A full-bridge, array-type loading system counterweight test was carried out to analyze the changes in the load values at the 6th, 11th, and 15th loading points. The results show that with the array-type loading system, the actual load at each point can reach the design value. Moreover, the self-balancing feature of the loading system can eliminate the impact of vertical deformation of the structure on the loading accuracy of each point, confirming the high reliability of the system.

(5) Using the ANSYS APDL software, finite element models of the original bridge and the model test bridge were established. Based on the counterweight optimization method proposed in this study, the counterweight load required at each loading point of the model bridge was calculated and applied. The stress results of the rigid steel frame, the concrete inside the pipe, and the externally wrapped concrete at the key sections of the two bridges were compared. The results show that the stress results of different components of the model bridge and the original bridge have basically the same trend at each construction stage. During the stage of casting web concrete, the stress of the rigid steel frame and the concrete inside the pipe of the model bridge was

slightly higher than that of the original bridge due to the increased self-weight load caused by the increase in the thickness of the model bridge's web from the design value of 45 mm to 55 mm. At other key construction stages, the maximum relative errors in the stress results of the rigid steel frame and the concrete inside the pipe for the two bridges are 8.33% and 9.34%, respectively. The maximum absolute error of the bottom plate concrete is 0.66 MPa, verifying the correctness of the counterweight optimization algorithm of the array-type, self-balancing pulley-group loading system.

It is worth mentioning that the loading point of this experiment considered the position of the columns on the original bridge arch, which can meet the simulation loading requirements of the arch structure. Considering the long-term behavior and failure mode of the structure under full bridge load, it will be the next research direction.

Author Contributions: Conceptualization, Y.F. and J.Z.; methodology, Y.F. and C.L.; software, Y.F.; validation, J.X., J.Y. and S.W.; formal analysis, Y.F.; investigation, J.Z.; resources, C.L.; data curation, J.X.; writing—original draft preparation, J.Y.; writing—review and editing, S.W.; visualization, Y.F.; supervision, J.Y.; project administration, J.X.; funding acquisition, J.Z. All authors have read and agreed to the published version of the manuscript.

Funding: This work was supported by Science and Technology Project of Chongqing Municipal Transportation Bureau (Grant No. KJXM2021-0966); Guangxi key research and development plan project (Grant No. GuikeAB22036007); Independent research and development project of the State Key Laboratory of Mountain Bridge and Tunnel Engineering (Grant No. SKLBT-YF2103); Project of Science and Technology Program of Department of Transport, Hubei Province (Grant No. 2020-186-1-6) and Chongqing Jiaotong University Postgraduate Scientific Research Innovation Project (Grant No. CYB22232).

Data Availability Statement: The data presented in this study are available from the first and corresponding author upon request. The data are not publicly available due to the policy of the data provider.

Conflicts of Interest: The authors declare no conflict of interest. The sponsors had no role in the design, execution, interpretation, or writing of the study.

References

1. Zheng, J. New development trend of long span concrete arch bridges in China. *J. Chongqing Jiaotong Univ. (Nat. Sci. Ed.)* **2016**, *35*, 8–11.
2. Xin, J.; Zhou, J.; Zhou, F.; Yang, S.X.; Zhou, Y. Bearing Capacity Model of Corroded RC Eccentric Compression Columns Based on Hermite Interpolation and Fourier Fitting. *Appl. Sci.* **2019**, *9*, 24. [CrossRef]
3. Hu, Z.; Zhang, M.; Kong, X.; Wu, D. Static and dynamic similarity model of long-span steel truss arch bridge. *Chin. J. Highw.* **2014**, *27*, 82–89.
4. Zong, Z.; Zhou, R.; Huang, X.; Xia, Z. Seismic response study on a multi-span cable-stayed bridge scale model under multi-support excitations. Part I: Shaking table tests. *J. Zhejiang Univ.-Sci. A* **2014**, *15*, 351–363. [CrossRef]
5. Chen, L.; Wu, H.; Fang, Q.; Li, R. Full-scale experimental study of a reinforced concrete bridge pier under truck collision. *J. Bridge Eng.* **2021**, *26*, 05021008. [CrossRef]
6. Zheng, W.; Sheng, X.; Zhu, Z.; Luo, T.; Liu, Z. Experimental study on vibration characteristics of unit-plate ballastless track systems laid on long-span bridges using full-scale test rigs. *Sensors* **2020**, *20*, 1744. [CrossRef]
7. Li, Z.; Zhao, C.; Shu, Y.; Deng, K.; Cui, B.; Su, Y. Full-scale test and simulation of a PBL anchorage system for suspension bridges. *Struct. Infrastruct. Eng.* **2020**, *16*, 452–464. [CrossRef]
8. Chen, B.; Wei, J.; Lin, J. Experimental study on spatial stress of concrete filled steel tubular (single tube) single rib arch. *Eng. Mech.* **2006**, *23*, 99–106.
9. Liu, Z.; Wang, S.; Xin, J.; Zhou, J.; Li, Y. Experimental study on failure of single-pipe arch of concrete-filled steel catenary pipe. *J. Railw. Sci. Eng.* **2022**, 1–11. [CrossRef]
10. Wang, G.; Xia, Q.; Wang, Y.; Liu, C.; Sun, D. Research on static performance of double deck corrugated steel concrete composite arch. *J. Build. Struc.* **2021**, *42* (Suppl. S2), 358–364.
11. Liu, A.; Zhang, J.; Zhao, X.; Li, Y.; Mei, L. Zhongshan First Bridge Model Test and Theoretical Analysis. *China Highw. J.* **2005**, *18*, 75–79+83.
12. Li, Y.; Wang, Y. Static model experiment study on a concrete-filled steel tubular arch bridge. *Key Eng. Mater.* **2015**, *648*, 61–71. [CrossRef]

13. Zhang, S.; Zhao, R.; Jia, Y.; Wang, Y.; Xie, H. Model test research on long-span high-speed railway rigid skeleton concrete arch bridge. *J. Southwest Jiaotong Univ.* **2017**, *52*, 1088–1096.
14. Tang, X.; Xie, J.; Zhao, S.; Dong, W.; Pu, Q.; Yang, Y.; Weng, H. Experimental study on reinforced concrete arch model of Wanxian Yangtze River Bridge. *J. Southwest Jiao Tong Univ.* **1994**, *29*, 362–367.
15. Li, C.; Liu, J.; Jiang, L. Theoretical analysis of gravity distortion and quality distortion on scale test error. *J. Railw. Sci. Eng.* **2022**, 1–9. [CrossRef]
16. Srinivas, V.; Sasmal, S.; Ramanjaneyulu, K.; Ravisankar, K. Performance evaluation of a stone masonry–arch railway bridge under increased axle loads. *J. Perform. Constr. Fac.* **2014**, *28*, 363–375. [CrossRef]
17. Alampalli, S.; Frangopol, D.M.; Grimson, J.; Halling, M.W.; Kosnik, D.E.; Lantsoght, E.O.; Zhou, Y.E. Bridge load testing: State-of-the-practice. *J. Bridge Eng.* **2021**, *26*, 03120002. [CrossRef]
18. Lu, P.; Xu, Z.; Chen, Y.; Zhou, Y. Prediction method of bridge static load test results based on Kriging model. *Eng. Struct.* **2020**, *214*, 110641. [CrossRef]
19. Commander, B. Evolution of bridge diagnostic load testing in the USA. *Front. Built Environ.* **2019**, *5*, 57. [CrossRef]
20. Feng, S.; Xiao, F. The design of Longtan Roller Compacted Concrete gravity dam. In *Roller Compacted Concrete Dams*; Routledge: London, UK, 2018; pp. 597–602.
21. Li, X.; Wang, M.; Xiao, J.; Zou, Q.; Liu, D. Experimental study on aerodynamic characteristics of high-speed train on a truss bridge: A moving model test. *J. Wind Eng. Ind. Aerod.* **2018**, *179*, 26–38. [CrossRef]
22. Zhang, C.; Jiang, G.; Su, L.; Lei, D.; Liu, W.; Wang, Z. Large-scale shaking table model test on seismic performance of bridge-pile-foundation slope with anti-sliding piles: A case study. *Bull. Eng. Geol. Environ.* **2020**, *79*, 1429–1447. [CrossRef]
23. Gusella, F.; Orlando, M. Analysis of the dissipative behavior of steel beams for braces in three-point bending. *Eng. Struct.* **2021**, *244*, 112717. [CrossRef]
24. He, Y. *Preparation and Performance Study of C60 Fine-Stone Self-Compacting Concrete Encased in Steel Tube Arch*; Chongqing Jiaotong University: Chongqing, China, 2022.
25. Carpinteri, A.; Corrado, M.; Mancini, G.; Mancini, G.; Paggi, M. Size-Scale Effects on Plastic Rotational Capacity of Reinforced Concrete Beams. *ACI Struct. J.* **2009**, *106*, 887–896.
26. Zhang, S.; Zhao, R.; Zhan, Y.; Xu, T.; Yang, X. Model test research on influence of shrinkage and creep on deformation of high-iron concrete arch bridge. *J. Chin. Railway Soc.* **2016**, *38*, 102–110.
27. Li, S.; Xin, J.; Jiang, Y.; Wang, C.; Zhou, J.; Yang, X. Temperature-induced deflection separation based on bridge deflection data using the TVFEMD-PE-KLD method. *J. Civ. Struct. Health Monit.* **2023**, *13*, 781–797. [CrossRef]
28. Wolny, S. Dynamic loading of the pulley block in a hoisting installation in normal operating conditions. *Arch. Min. Sci.* **2009**, *54*, 261–284.
29. Liu, Y.; Jing, X.; Wan, Y. Structural Design and Simulation of Ejection Device with Pulley Block. In *2019 2nd International Conference on Mathematics, Modeling and Simulation Technologies and Applications (MMSTA 2019)*; Atlantis Press: Amsterdam, The Netherlands, 2019; pp. 26–29.
30. Reutov, A.A.; Kobishchanov, V.V.; Sakalo, V.I. Dynamic modeling of lift hoisting mechanism block pulley. *Procedia Eng.* **2016**, *150*, 1303–1310. [CrossRef]
31. ANSYS. *Structural Finite Element Analysis (FEA) Software*; ANSYS Inc.: Canonsburg, PA, USA, 2023.